Facile synthesis of Bi₂MoO₆–MIL-100(Fe) metal–organic framework composites with enhanced photocatalytic performance

Jia Yang,[abc] Xiaojun Niu,*[abcd] Shaorong An,[abc] Weiyi Chen,[abc] Jie Wang[abc] and Wei Liu[abc]

A novel Bi_2MoO_6–MIL-100(Fe) heterostructure photocatalyst was synthesized by a facile solvothermal method for the first time, and characterized by X-ray diffraction, scanning electron microscopy, X-ray photoelectron spectroscopy, UV-vis diffuse reflectance spectra, transmission electron microscopy, and photoluminescence spectra. The as-prepared Bi_2MoO_6–MIL-100(Fe) composites exhibited excellent photocatalytic activity and stability towards the degradation of Rhodamine B (RhB) under visible light irradiation. The introduction of MIL-100(Fe) into semiconductor Bi_2MoO_6 improved the photocatalytic performance remarkably, and the optimal composite with 9% MIL-100(Fe) content showed the highest photocatalytic activity. According to the active radical trapping experiments, the h^+ and $\cdot O_2^-$ radicals were the two main active species in the photocatalytic reaction. The enhanced photocatalytic performance is mainly attributed to the formation of the Bi_2MoO_6–MIL-100(Fe) heterostructure, which is beneficial to the transfer and separation of photo-generated electron–hole pairs. The possible mechanism of the enhanced photocatalytic performance of the Bi_2MoO_6–MIL-100(Fe) composites was discussed.

1. Introduction

The semiconductor photocatalysis technique has attracted extensive attention in the splitting of water and the degradation of organic pollutants using sunlight as the energy source.[1] Among the various photocatalysts, TiO_2 is an attractive photocatalyst, because of its low toxicity, high photocatalytic activity and long term chemical stability.[2–4] However, the applications of TiO_2 are severely limited, owing to it only being excited by ultraviolet (UV) light which accounts for less than 5% of the solar spectrum. Therefore, many reports are focused on developing visible light responsive photocatalytic materials to replace TiO_2, such as Bi_2MoO_6,[5] In_2O_3,[6] Ag_3PO_4,[7] and g-C_3N_4 (ref. 8) photocatalysts.

Bi_2MoO_6 is a typical Aurivillius oxide, exhibited excellent photocatalytic activity under the visible light irradiation.[9] Compared with TiO_2, Bi_2MoO_6 has a lower band gap (2.5–

2.8 eV), which makes it utilize more sunlight and displays remarkable photocatalytic performance for organic pollutant degradation under visible light irradiation.[10] However, the practical application of the pure phase Bi_2MoO_6 is limited by its poor quantum yield, which is caused by the rapid recombination of photoinduced charge carriers. To further improve the photocatalytic activity of Bi_2MoO_6, many feasible methods have been explored, including designing textural properties, doping composites[11,12] and combining with other semiconductors,[13–15] carbon materials[16] or noble metals.[17] Nevertheless, there is still plenty of space to explore unfulfilled potentials for fabricating Bi_2MoO_6-based photocatalysts.

Metal–organic frameworks (MOFs) are an extensive class of crystalline materials formed by the self-assembly between metal ions and organic ligands.[18] Recently, they have obtained extensive attention owing to their huge potential applications in sensing,[19] gas storage,[20] drug delivery,[21] optical properties[22] and catalysis. These MOFs composites can act as catalysts, using unsaturated metal sites and catalytically active organic likers.[23,24] Additionally, MOFs exhibit tunable photo-physical and photo-chemical properties, it can work well as excellent candidates for photocatalysis. For example, Dan-Hardi *et al.* synthesized a new photoactive crystalline titanium dicarboxylate (MIL-125(Ti)), which exhibits high photonic sensitivity under UV-visible irradiation.[25] Hou Wang *et al.* had reported that $In_2S_3@MIL-125(Ti)$ can remove the tetracycline by adsorption and photocatalysis. These reports showed that some MOFs can

ᵃSchool of Environment and Energy, College of Environment and Energy, South China University of Technology, Guangzhou, 510006, China. E-mail: xjniu@scut.edu.cn; Fax: +86-20-3934-9919; Tel: +86-20-3934-9919

ᵇGuangdong Provincial Key Laboratory of Atmospheric Environment and Pollution Control, Guangzhou Higher Education Mega Centre, Guangzhou 510006, PR China

ᶜThe Key Lab of Pollution Control and Ecosystem Restoration in Industry Clusters, Ministry of Education, South China University of Technology, Guangzhou Higher Education Mega Centre, Guangzhou 510006, PR China

ᵈThe State Key Laboratory of Lake Science and Environment, Nanjing Institute of Geography and Limnology, Chinese Academy of Sciences, Nanjing, 210008, PR China

be applied in photocatalysis.[26] Compared with traditional semiconductor photocatalysts, the superiority of MOFs is their ultrahigh surface area and narrow micropore distribution which may lead to the formation of monodisperse photoactive species supported on MOFs.[27] Recently, several semi-conductor@MOF heterostructures like CdS@MIL-100(Fe),[28] CdS@UiO-66(NH$_2$),[18] ZnO@ZIF-8,[29] and GaN@ZIF-8 (ref. 30) have been synthesized and exhibited excellent catalytic performance due to their synergistic effect. However, the photocatalytic performance of Bi$_2$MoO$_6$–MOF composites, to the best of our knowledge, has not been investigated.

Herein, we report a novel Bi$_2$MoO$_6$–MIL-100(Fe) composite that shows excellent photocatalytic activity in degradation organic pollutants. A series of Bi$_2$MoO$_6$–MIL-100(Fe) composites with different weight addition ratios of MIL-100(Fe) have been successfully synthesized via a facile solvothermal method. The photocatalytic performance was evaluated by the degradation of Rhodamine B under visible light irradiation. The combination of MIL-100(Fe) remarkably improved the photostability and the photocatalytic efficiency of the photocatalyst for degradation RhB. Furthermore, the possible mechanism of the enhanced photocatalytic performance of the Bi$_2$MoO$_6$–MIL-100(Fe) composite was discussed.

2. Experimental

2.1 Materials

Bismuth nitrate pentahydrate, sodium molybdate dehydrate were obtained from Tianjin Kemiou Chemical Reagent Co., Ltd. (Tianjin, China), benzene-1,3,5-tricarboxylic acid (H$_3$btc) and Fe powder were purchased from Aladdin Industrial Corporation (Shanghai, China). Ethylene glycol (EG), and ethanol (EtOH) were purchased from Sinopharm Chemical Reagent Co., Ltd. (Shanghai, China). All chemicals were analytic grade and used without further purification.

2.2 Preparation of MIL-100(Fe)

According to the previous literature,[31,32] MIL-100(Fe) was prepared by solvothermal method. In detail, a mixture of Fe powder with H$_3$btc, HF, HNO$_3$ and H$_2$O with a molar ratio of 1 : 0.67 : 2 : 0.6 : 2.77 was synthesized in a Teflon-lined stainless steel autoclave at 150 °C for 24 h. Then the orange solid was centrifuged, washed with ethanol and hot water for several times, and finally dried overnight 60 °C under vacuum.

2.3 Synthesis of Bi$_2$MoO$_6$–MIL-100(Fe) composite

The as-prepared MIL-100(Fe) with the desired weight addition was dispersed in 10 mL ethanol by ultrasonication to gain the homogeneous MIL-100(Fe)–EtOH dispersion. Next, 2 mmol Bi(NO$_3$)$_3$·5H$_2$O and 1 mmol Na$_2$MoO$_4$·2H$_2$O dissolved in 20 mL ethylene glycol were dropwised into MIL-100(Fe)–EtOH dispersion. After being stirred for 30 min at room temperature, the mixed solution was transferred into a 50 mL Teflon-lined stainless steel autoclave and kept at 160 °C for 12 h. Finally, the obtain samples were collected, washed with deionized water and ethanol, dried overnight at 60 °C under vacuum. According

to the method, as-synthesized composites with expected MIL-100(Fe) contents of 3, 6, 9 and 12% were synthesized and named as Bi$_2$MoO$_6$–MIL-100(Fe)-3, Bi$_2$MoO$_6$–MIL-100(Fe)-6, Bi$_2$MoO$_6$–MIL-100(Fe)-9 and Bi$_2$MoO$_6$–MIL-100(Fe)-12, respectively. For comparison, the Bi$_2$MoO$_6$–MIL-100(Fe) physical mixture composites were synthesized by simple mechanical mixture, and named as Bi$_2$MoO$_6$–MIL-100(Fe)-9(M). As a control, pure Bi$_2$MoO$_6$ was also prepared in ethanol under the same reaction conditions as that of Bi$_2$MoO$_6$–MIL-100(Fe) composites except for the addition of MIL-100(Fe).

2.4 Characterization

X-ray diffraction (XRD) patterns of all samples were carried out using an Empyrean diffractometer (PANalytical B.V., Netherlands), with Cu Kα radiation (λ = 1.54184 Å) in the 2θ range of 10–80°. The morphologies and microstructures of the products were characterized by a Merlin field emission scanning electron microscope (FE-SEM, Zeiss). Transmission electron microscopy (TEM) images and high-resolution transmission electron microscopy (HRTEM) images were obtained by FEI Tecnai G2 F20 microscope at an accelerating voltage of 200 kV. The Brunauer–Emmett–Teller (BET) surface area was examined by nitrogen adsorption–desorption isotherm at 77 K on Micromeritics Instrument 3Flex adsorption analyzer. X-ray photoelectron spectroscopy (XPS) was performed on a Thermo Escalb 250Xi spectrometer with a monochromatic Al (Kα) radiation. The UV-vis diffuse reflectance spectra (DRS) of samples were measured with Hitachi U-4100 UV-vis spectrophotometer. The photoluminescence (PL) spectra were tested with an FLS 920 FluorescencLe spectrometer at room temperature.

2.5 Photocatalytic evaluation

The photocatalytic activity of samples was evaluated by the degradation of Rhodamine B (RhB). In experiments, 0.1 g samples were added to 100 mL aqueous solution of RhB (10 mg L^{-1}) in a BL-GHX photochemical reactor (Shanghai Bilon Instrument. ltd. China). A 500 W Xe lamp was used as the visible-light source with 420 nm cut-off filter. Before irradiation, the suspension was kept in the dark under stirring for 30 min to ensure an adsorption–desorption equilibrium. After a given irradiation, about 4 mL suspension was collected, centrifuged and analyzed immediately. The RhB concentration were analyzed by a UV-vis spectrometer (Agilent 8453, USA) at 554. The TOC concentration was analyzed by Shimadzu TOC-LCPN analyzer. The degradation efficiency (%) was calculated as follows:

$$\text{Degradation (\%)} = \frac{(C_0 - C)}{C_0} \times 100\% \tag{1}$$

where C_0 is the initial concentration of RhB, and C is the time-dependent concentration of RhB upon irradiation.

3. Results and discussion

3.1 XRD analyses

The crystal structures of the as-synthesized samples were examined by XRD patterns. Fig. 1 shows the XRD patterns of
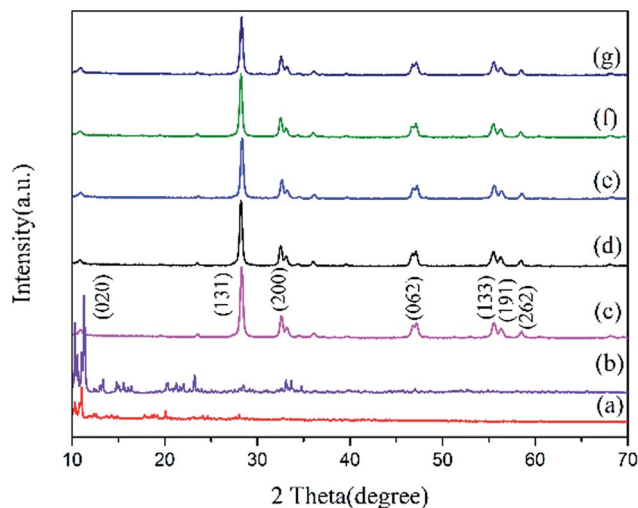
Fig. 1 XRD patterns of (a) MIL-100(Fe), (b) MIL-100(Fe)-simulated, (c) Bi_2MoO_6, (d) Bi_2MoO_6–MIL-100(Fe)-3, (e) Bi_2MoO_6–MIL-100(Fe)-6, (f) Bi_2MoO_6–MIL-100(Fe)-9, (g) Bi_2MoO_6–MIL-100(Fe)-12.

Bi_2MoO_6, and Bi_2MoO_6–MIL-100(Fe) composites with different contents of MIL-100(Fe). For comparison, the patterns of pure MIL-100(Fe), Bi_2MoO_6 as well as simulated MIL-100(Fe) are also shown. These distinct diffraction peaks at $2\theta = 10.85, 28.2, 32.5, 46.7$ and $55.5°$, can be attributed to the (020), (131), (200), (062) and (133) crystal planes of pure Bi_2MoO_6 (JCPDS 76-2388). The diffraction peaks of pure MIL-100(Fe) sample can match with simulated MIL-100(Fe), the XRD result indicated the structure of pure MIL-100(Fe) sample is intact. For the Bi_2MoO_6–MIL-100(Fe) samples (Fig. 1d–g), all diffraction peaks indexed to the orthorhombic Bi_2MoO_6 phase are clearly observed. However, no peak in samples assigned to MIL-100(Fe) was observed, possibly due to the low content and high dispersion of MIL-100(Fe). In addition, no impurity was observed. With the increase of MIL-100(Fe) contents, the intensities of peaks for Bi_2MoO_6 get reduced.

3.2 Morphology

Fig. 2 shows the SEM images of Bi_2MoO_6, MIL-100(Fe) and their composites Bi_2MoO_6–MIL-100(Fe)-9, respectively. The rough microspheres composed of nanoparticles with dozens of nanometers are observed for Bi_2MoO_6 (Fig. 2a). And the diameter of the microsphere is 1–3 μm. In the Fig. 2b, the pure MIL-100(Fe) exhibited regular octahedron morphology with diameter ranging from 2 to 4 μm. As for the Bi_2MoO_6–MIL-100(Fe)-9 composite (Fig. 2c and d), it can be observed that MIL-100(Fe) serves as a support and the nanoparticles of Bi_2MoO_6 grow on the surface of MIL-100(Fe). Meanwhile, there is no aggregation of Bi_2MoO_6 nanoparticles on MIL-100(Fe), indicating that the interaction between Bi_2MoO_6 and MIL-100(Fe) is strong. Besides, the regular octahedron morphology of MIL-100(Fe) was not changed in the composite, the result demonstrated the structure of MIL-100(Fe) was not destroyed in the synthesized process of Bi_2MoO_6–MIL-100(Fe) composite. The Energy Dispersive Spectroscopy (EDS) patterns of Bi_2MoO_6–MIL-

100(Fe)-9 composite revealed the existence of Bi, Mo, C, O and Fe. The tight interaction between the Bi_2MoO_6 and MIL-100(Fe) can enhance the photocatalytic activity.

The TEM and HRTEM images of Bi_2MoO_6–MIL-100(Fe)-9 sample were shown in Fig. 3a and b, respectively. The TEM image shows the Bi_2MoO_6 nanoparticles on the MIL-100(Fe) surface, and the microstructures of the Bi_2MoO_6–MIL-100(Fe)-9 sample. The HRTEM images clearly indicated the resolved lattice fringes of 0.315, 0.406 and 0.192 nm, which correspond to the (131), (040) and (062) planes of orthorhombic phase of Bi_2MoO_6, respectively. The results indicate that the formation of composites of Bi_2MoO_6 and MIL-100(Fe) can promote faster separation of photoinduced charge carriers and improve photocatalytic activities.

3.3 XPS analysis

The surface chemical composition of Bi_2MoO_6–MIL-100(Fe)-9 was analyzed by XPS. Fig. 4 shows XPS survey spectra and high-resolution XPS spectra of the Bi 4f, Mo 3d, O 1s, Fe 2p and C 1s regions for the sample of Bi_2MoO_6–MIL-100(Fe)-9. The survey spectra indicated that Bi, Mo, O, Fe and C exist on the surface of Bi_2MoO_6–MIL-100(Fe)-9, and no impurities were detected, in accordance with EDS result. In the Bi 4f spectrum, two peaks at 159.2 eV and 164.5 eV are attributed to Bi $4f_{7/2}$ and Bi $4f_{5/2}$ of Bi^{3+}, respectively.[33] In the Mo 3d spectrum, peaks at 232.5 eV and 235.6 eV were ascribed to Mo $3d_{5/2}$ and Mo $3d_{3/2}$ of Mo^{6+}, respectively.[34] The O 1s peak of the composite at 530.1 eV is observed, which was relate to Mo–O.[35] The Fe 2p peak was associated with the binding energy at 712.1 eV, which are characteristic of Fe(III) in MIL-100(Fe).[31] In addition, the C 1s peaks at 288.8 and 284.7 eV arises from MIL-100(Fe) and external carbon contamination, respectively.[36] In summary, the XPS spectra analysis confirms that Bi_2MoO_6–MIL-100(Fe) composites have been synthesized successfully.

3.4 BET analysis

Brunauer–Emmett–Teller (BET) surface area of the as-synthesized samples were examined by nitrogen adsorption–desorption isotherms at 77 K. It can be found that the introduction of MIL-100(Fe) can significantly affect the BET surface area of samples. Compared with pure Bi_2MoO_6, the BET surface area (S_{BET}) of Bi_2MoO_6–MIL-100(Fe) composites obviously increased, from 9.3172 m^2 g^{-1} to 109.6347 m^2 g^{-1}. The larger surface area of photocatalysts can provide more surface active sites and promote charge carriers transport easily, contributing to an enhanced photocatalytic performance.[37] Therefore, MIL-100(Fe) in synthesized composites may play the key role in enhancing the photocatalytic activity.

3.5 PL analysis

Photoluminescence (PL) spectra were used to investigate the transfer and separation efficiency of photogenerated electron–hole pairs.[38] As we all known, the lower PL intensity indicated a lower recombination of photoinduced charge carriers. The PL spectra of Bi_2MoO_6, MIL-100(Fe) and Bi_2MoO_6–MIL-100(Fe)-9 for excitation wavelength 605 nm are shown in Fig. 5. The
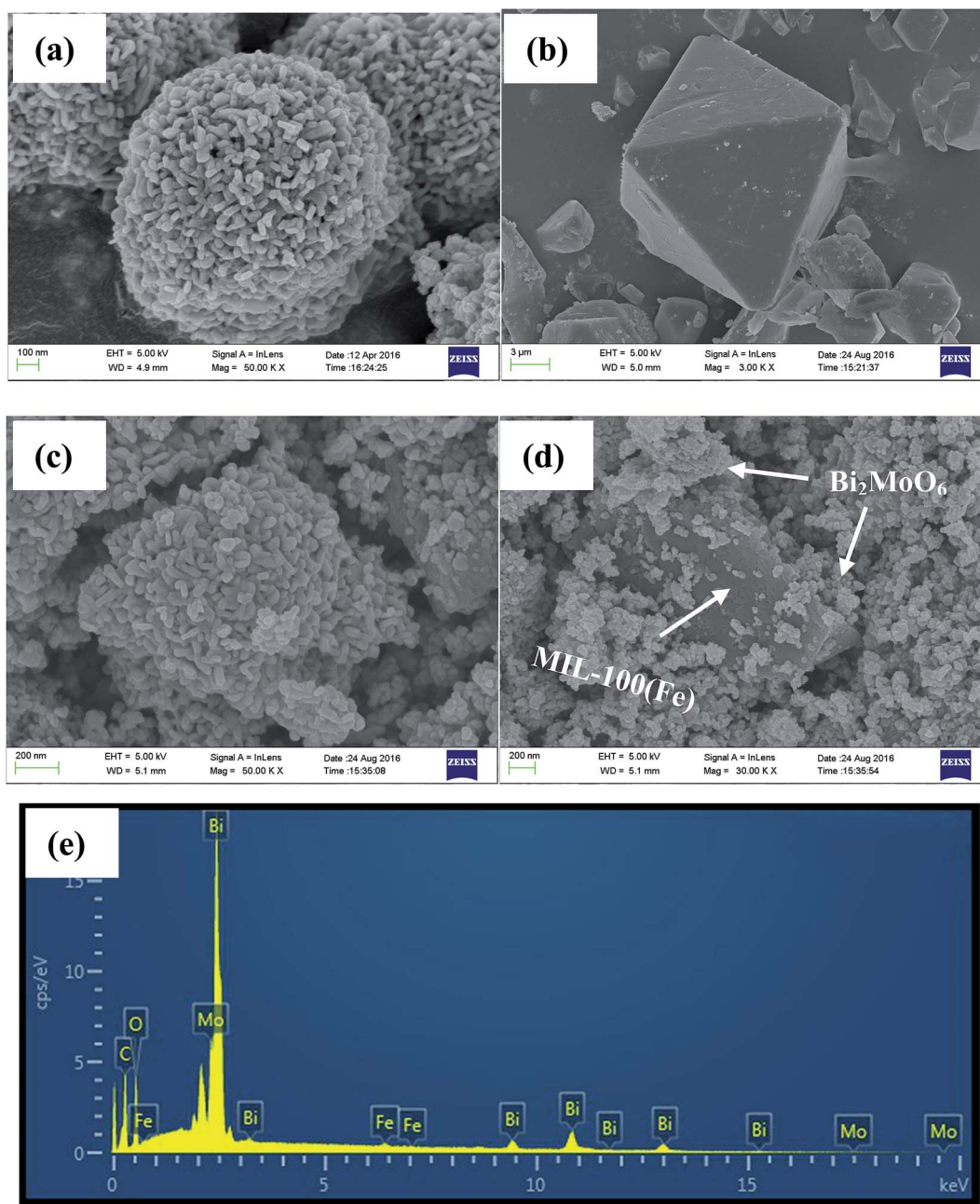
Fig. 2 SEM images of (a) pure Bi_2MoO_6, (b) pure MIL-100(Fe), (c) and (d) Bi_2MoO_6–MIL-100(Fe)-9 composites, and (e) EDS patterns of the Bi_2MoO_6–MIL-100(Fe)-9 composites.

main emission peaks around 460–500 nm appear for three photocatalysts, and the emission peak of Bi_2MoO_6–MIL-100(Fe)-9 is lower than the Bi_2MoO_6 and MIL-100(Fe). The resulting of the PL spectra indicated the addition of MIL-100(Fe) into semiconductor Bi_2MoO_6 is contributed to the separation of photo-generated electron–hole pairs.

3.6 UV-vis DRS

The UV-vis diffusive reflectance spectra (UV-vis DRS) of Bi_2MoO_6, MIL-100(Fe) and Bi_2MoO_6–MIL-100(Fe)-9 photocatalysts were shown in Fig. 6a. The adsorption of three

photocatalytic samples are located in visible light region. The absorption edge of Bi_2MoO_6 is 485 nm, and MIL-100(Fe) exhibits absorption edge in 550 nm. As the composites of two different semiconductors, the Bi_2MoO_6–MIL-100(Fe)-9 exhibits absorption edges at 510 nm. Furthermore, the band gap energies of Bi_2MoO_6 and MIL-100(Fe) could be calculated by the following equation:[39]

$$\alpha(h\nu) = A(h\nu - E_g)^{1/2} \tag{2}$$

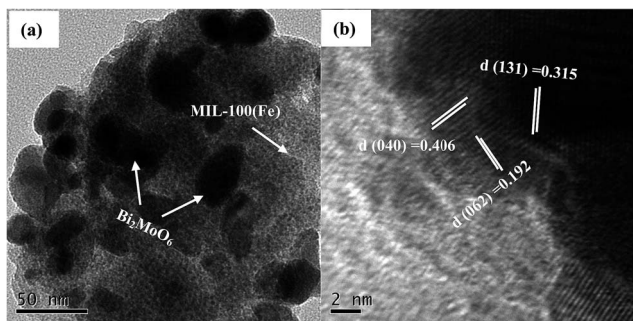where α, ν, E_g, and A are the absorption coefficient, the light frequency, the energy band gap of semiconductor, and

Fig. 3 (a) TEM and (b) HRTEM images of Bi_2MoO_6–MIL-100(Fe)-9.

a constant, respectively. According to eqn (2), the band-gap of photocatalysts can be estimated from plots of $(\alpha h\nu)^2$ *versus* energy ($h\nu$). In the Fig. 6b, the band gaps of as-synthesized Bi_2MoO_6, MIL-100(Fe) and Bi_2MoO_6–MIL-100(Fe)-9 are estimated to be 2.58, 2.50 and 2.38 eV, respectively. The resulting confirmed that Bi_2MoO_6 can match up with MIL-100(Fe)
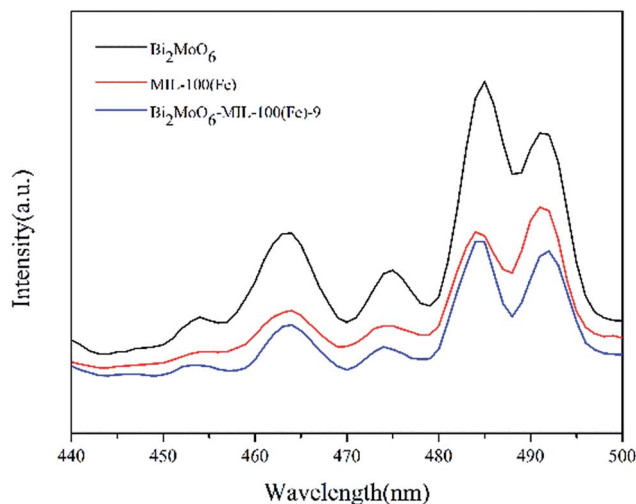

Fig. 5 PL spectra of Bi_2MoO_6, MIL-100(Fe) and Bi_2MoO_6–MIL-100(Fe)-9, recorded at an excitation wavelength of 605 nm.
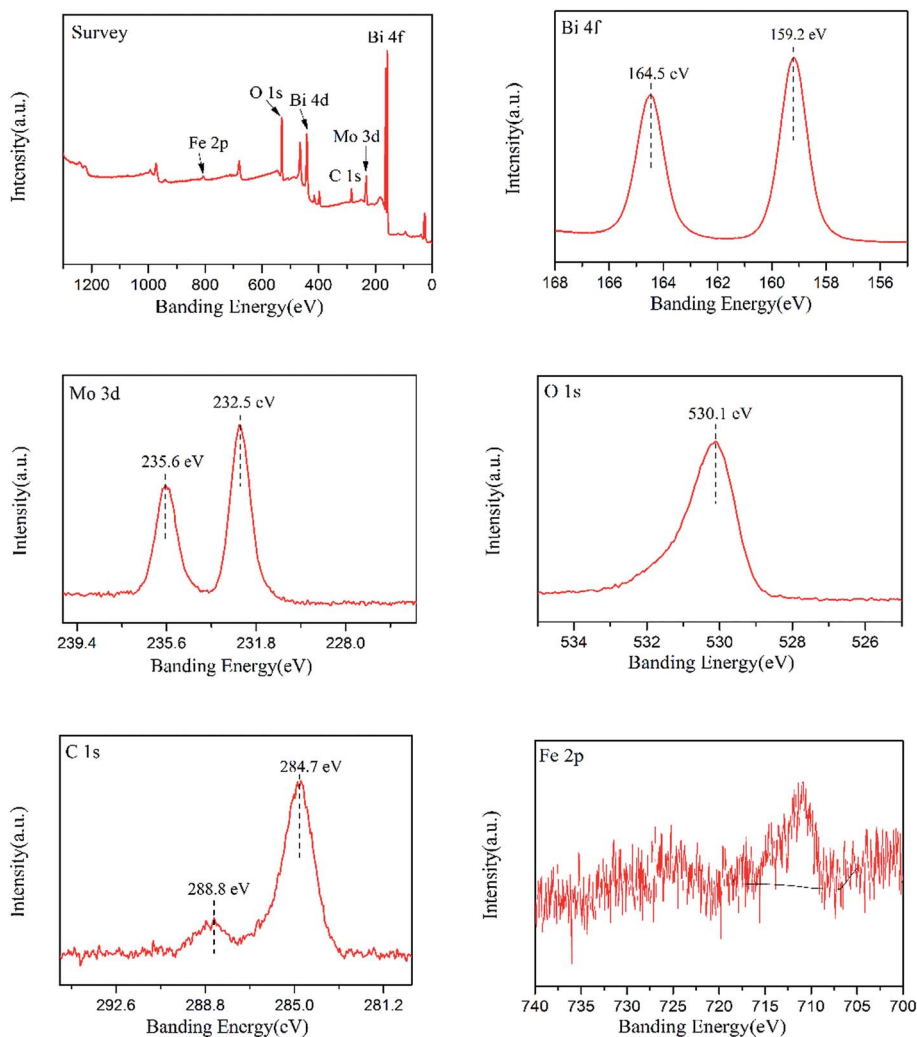
Fig. 4 XPS survey spectra of Bi_2MoO_6–MIL-100(Fe)-9 and high-resolution XPS spectra of the Bi 4f, Mo 3d, O 1s, Fe 2p and C 1s.

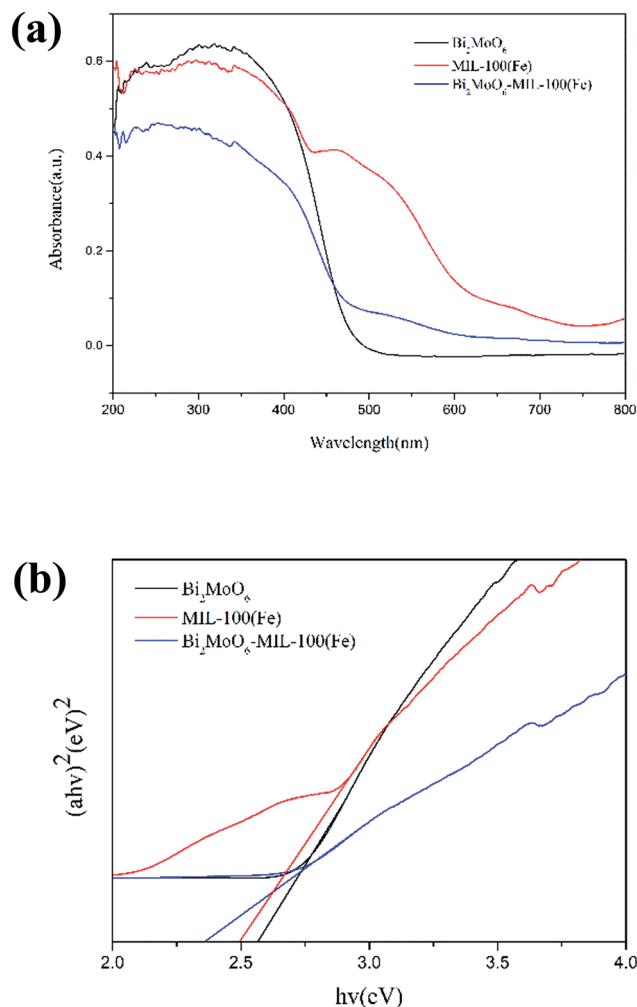Fig. 6 (a) UV-vis diffuse reflectance spectra (DRS) of Bi$_2$MoO$_6$, MIL-100(Fe) and Bi$_2$MoO$_6$–MIL-100(Fe)-9; (b) the plots of (ahv)$^{n/2}$ vs. photon energy (hv) for the band-gap energies of Bi$_2$MoO$_6$, MIL-100(Fe) and Bi$_2$MoO$_6$–MIL-100(Fe)-9.

Fig. 7 (a) Photodegradation of as-prepared samples for RhB. (b) The kinetic constants (k) of photocatalytic for RhB.

perfectly, which contributes to the separation of the electron–hole pairs.

3.7 Photocatalytic activity

The photocatalytic activities of as-prepared photocatalysts were evaluated by the degradation of RhB under visible light irradiation. The RhB adsorption and photodegradation process of different photocatalysts are shown in Fig. 7a. Before the visible light irradiation, the absorption–desorption balance has been reached between the catalyst and RhB for 30 min absorption process. Fig. 7a shows that RhB was hardly decomposed by photolysis without any catalysts under visible light irradiation. The adsorption rate of pure Bi$_2$MoO$_6$ and MIL-100(Fe) are 15.36% and 44.39% in the dark, respectively. The adsorption rate of MIL-100(Fe) is very high, but it has low photocatalytic performance for RhB under the visible-light irradiation. Meanwhile, pure Bi$_2$MoO$_6$ shows low photocatalytic activity for RhB degradation, the photodegradation rate is 62.56%.
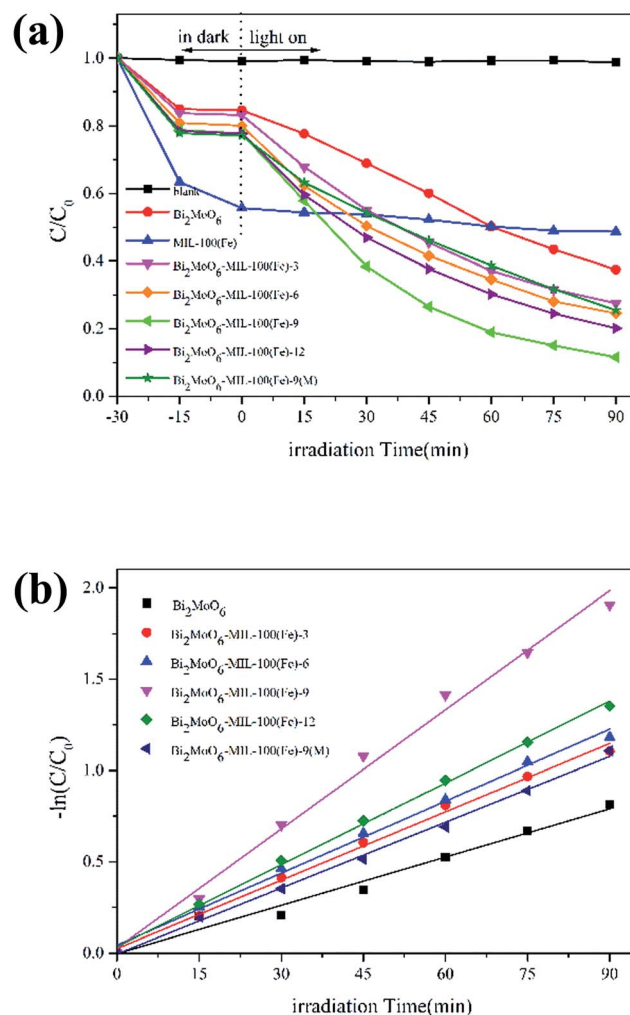
However, the addition of MIL-100(Fe) improved the photocatalytic activities of Bi$_2$MoO$_6$–MIL-100(Fe) composites significantly. The photocatalytic activities of Bi$_2$MoO$_6$–MIL-100(Fe) composites enhanced, with the increase of content of MIL-100(Fe). When the addition of MIL-100(Fe) reached 9%, Bi$_2$MoO$_6$–MIL-100(Fe) composites demonstrated greater degradation performance, up to 88.46% RhB removed in 120 min. Meanwhile, the absorption of RhB in Bi$_2$MoO$_6$–MIL-100(Fe)-9 increased to 22.25% compared with pure Bi$_2$MoO$_6$, indicating that the introduction of MIL-100(Fe) promoted the increase of adsorption ability of catalysts. Besides, the physical mixture Bi$_2$MoO$_6$–MIL-100(Fe)-9(M) composite exhibited lower activity than Bi$_2$MoO$_6$–MIL-100(Fe)-9, it may be due to the instable Bi$_2$MoO$_6$–MIL-100(Fe) heterojunctions. The result indicated that the presence of MIL-100(Fe) enhanced light absorption, separation of photo-generated electron–hole pairs, and increased surface area. The enhanced photocatalytic performance is contributed to the heterostructure between Bi$_2$MoO$_6$ and MIL-100(Fe). In addition, Fig. 7b shows the corresponding first-order kinetics plot by the equation:[40]

$$-\ln(C/C_0) = kt \qquad (3)$$

where C_0 and C are the RhB concentrations in solution at times 0 and t, respectively, and k is the apparent first-order rate constant. According to the equation, the rates of RhB degradation are 0.00881 min^{-1}, 0.01248 min^{-1}, 0.01314 min^{-1}, 0.02174 min^{-1}, 0.01494 min^{-1} and 0.01201 min^{-1} for pure Bi_2MoO_6, Bi_2MoO_6–MIL-100(Fe)-3, Bi_2MoO_6–MIL-100(Fe)-6, Bi_2MoO_6–MIL-100(Fe)-9, Bi_2MoO_6–MIL-100(Fe)-12 and Bi_2MoO_6–MIL-100(Fe)-9(M). The rate of RhB degradation of Bi_2MoO_6–MIL-100(Fe)-9 is higher than other photocatalysts. The result indicated that the interaction between Bi_2MoO_6 and MIL-100(Fe) can improve the photocatalytic performance, and the photocatalytic activity is significantly enhancing with the increase of the mass ratio of MIL-100(Fe). The photocatalytic activity reached the maximum value, when the mass ratio of MIL-100(Fe) is 9%.

The mineralization rate of RhB over photocatalysts was detected by Total Organic Carbon (TOC) test. The TOC results (Fig. 8) indicated that only 67.42% of RhB is mineralized over Bi_2MoO_6–MIL-100(Fe)-9 after 120 min and more irradiation time is needed to make the substrate completely mineralized. After 210 min, the mineralization rate of RhB over Bi_2MoO_6–MIL-100(Fe)-9 can only reach 87.29%. But the mineralization rate of RhB over Bi_2MoO_6–MIL-100(Fe)-9 is higher than that over Bi_2MoO_6 and Bi_2MoO_6–MIL-100(Fe)-9(M). The above results show that Bi_2MoO_6–MIL-100(Fe) composites exhibited much higher photocatalytic performance than pure Bi_2MoO_6 under visible light irradiation.

3.8 The proposed photocatalytic mechanism

3.8.1 Analysis of active species.
The active species including holes (h$^+$), superoxide radical ($^{\bullet}O_2^-$), and hydroxyl radicals ($^{\bullet}OH$) are possibly impact factors for the photodegradation of organic pollutants. It is important to carry out the trapping experiments for confirming the main active species generated over Bi_2MoO_6–MIL-100(Fe) composites. In the detection, EDTA-2Na (ref. 33) and *tert*-butyl alcohol (TBA)[41] are used as the scavengers of holes (h$^+$)

and hydroxyl radical ($^{\bullet}OH$). The *p*-benzoquinone (BQ)[42] and N$_2$ (ref. 43) are used as the scavenger of superoxide radical ($^{\bullet}O_2^-$). As shown in Fig. 9, the photocatalytic degradation of RhB over Bi_2MoO_6–MIL-100(Fe)-9 was slightly affected by the addition of TBA (1 mL). However, the photocatalytic activity of Bi_2MoO_6–MIL-100(Fe)-9 was significantly inhibited by the addition of EDTA-2Na (0.5 mmol). Similarly, the degradation rate was obviously decreased after the addition of BQ (0.5 mmol). In the word, active species including h$^+$ and $^{\bullet}O_2^-$ play the crucial roles in the photodegradation of pollutants.

To test the role of dissolved O$_2$ in the reaction process, enough nitrogen (N$_2$) was bubbled into the suspension to ensure that the degradation system was operated under anoxic conditions. In the presence of N$_2$, the photocatalytic activity of catalyst was inhibited under the same condition. This result means that dissolved O$_2$ is a vital factor in RhB removal over Bi_2MoO_6–MIL-100(Fe) composites, which affects the formation of $^{\bullet}O_2^-$ *via* direct reduction of O$_2$ and the formation of $^{\bullet}OH$ *via* indirect reduction of O$_2$.[44]

3.8.2 The proposed photocatalytic mechanism.
It is well-known that the photocatalytic performances of catalysts rely on the transfer, separation and generation of electron–hole pairs. In our study, the interaction between Bi_2MoO_6 and MIL-100(Fe) can promote the separation of photogenerated charge carries and improve the photodegradation rate under visible light. In order to understand the photocatalytic mechanism of the Bi_2MoO_6–MIL-100(Fe) composites in depth, the initial energy band structures of Bi_2MoO_6 and MIL-100(Fe) were estimated. The band edges of Bi_2MoO_6 and MIL-100(Fe) were calculated by the following empirical formulas:[45]

$$E_{VB} = X - E_e + 0.5E_g \qquad (4)$$

$$E_{CB} = E_{VB} - E_g \qquad (5)$$

where E_{VB} is the valence band (VB) edge potential, E_{CB} is the conduction band edge potential, E_g is the band gap energy of the semiconductor, X is the electronegativity of the
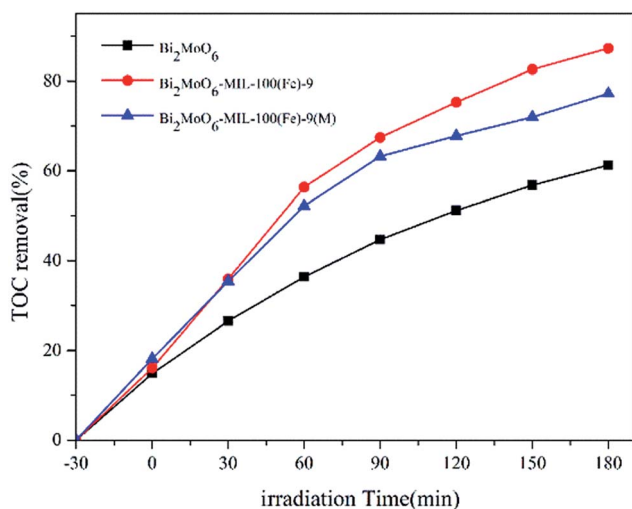

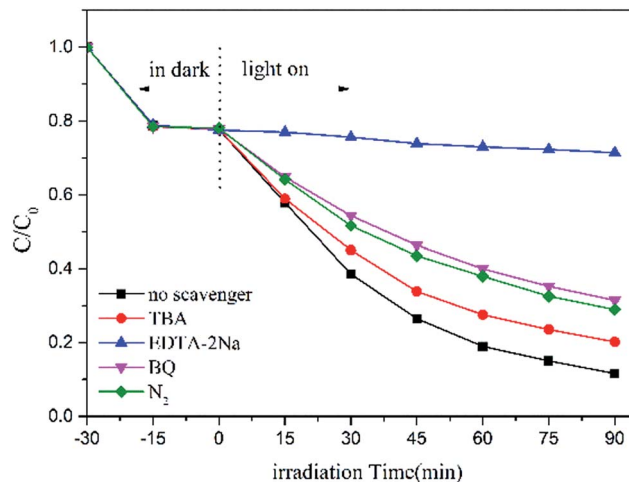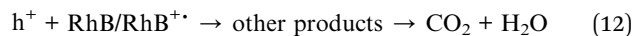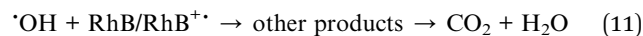Fig. 8 TOC removal process of RhB solution.

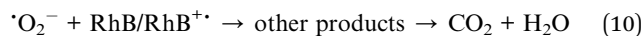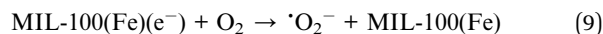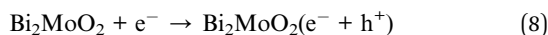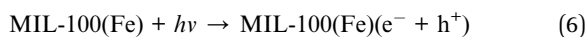Fig. 9 Photocatalytic degradation of RhB over Bi_2MoO_6–MIL-100(Fe)-9 with different scavengers.

semiconductor, which is the geometric mean of the electronegativity of the constituent atoms, and the X values for Bi_2MoO_6 and MIL-100(Fe) were calculated to be 5.55 and 5.10 eV, respectively. E_e is the energy of free electrons on the hydrogen scale (about 4.5 eV). The E_g of Bi_2MoO_6 and MIL-100(Fe) are estimated as 2.58 and 2.50 eV. According to above formulas, the VB and CB edge potentials of Bi_2MoO_6 are located at −0.24 and 2.34 eV, respectively. The VB and CB edge potentials of MIL-100(Fe) are determined to be −0.65 and 1.85 eV, respectively.

On the basis of above band energy level analysis and active species trapping detection, the possible proposed mechanism was discussed as illustrated in Scheme 1. Under the visible light irradiation, both Bi_2MoO_6 and MIL-100(Fe) can be excited for generation of electrons (e^-) and holes (h^+) in their CB and VB. The photo-generated electrons in the CB of MIL-100(Fe) transfer to the CB of Bi_2MoO_6 *via* the heterojunction structure. At the same, the holes in the VB of Bi_2MoO_6 can migrate to the VB of MIL-100(Fe), hence promoting the separation of photoinduced electron–holes pairs. O_2 molecules in solution adsorbed onto catalysts form superoxide radical ($\cdot O_2^-$) *via* electron transfer from MIL-100(Fe) to O_2, since the conduction band potential of MIL-100(Fe) (−0.65 eV *versus* NHE) was more negative than the standard redox potentials of ($E(O_2/\cdot O_2^-) = -0.33$ eV *versus* NHE). Similarly, the standard redox potentials of ($E(H_2O/\cdot OH) = +2.8$ eV *versus* NHE) was more positive than the VB of the Bi_2MoO_6 (2.34 eV) and MIL-100(Fe) (1.85 eV), thus it is difficult to oxidize the adsorbed H_2O into $\cdot OH$ for photo-generated. The part h^+ radicals reacted with H_2O molecules in solution to generate reactive hydroxyl ($\cdot OH$) and H^+ ions. Moreover, the adsorbed RhB onto Bi_2MoO_6–MIL-100(Fe) can be excited to RhB* under visible-light irradiation.[46] Then the electrons from RhB* are transformed into photocatalyst to form $RhB^{+\cdot}$. The RhB (or $RhB^{+\cdot}$) is finally photodegraded by the reactive species (O_2, $\cdot OH$) or h^+ to generate H_2O and CO_2. According to above discussion, the process can be described as follows:

$$MIL\text{-}100(Fe) + hv \rightarrow MIL\text{-}100(Fe)(e^- + h^+) \qquad (6)$$

$$RhB + hv \rightarrow RhB^* \rightarrow RhB^{+\cdot} + e^- \qquad (7)$$

$$Bi_2MoO_2 + e^- \rightarrow Bi_2MoO_2(e^- + h^+) \qquad (8)$$

$$MIL\text{-}100(Fe)(e^-) + O_2 \rightarrow \cdot O_2^- + MIL\text{-}100(Fe) \qquad (9)$$

$$\cdot O_2^- + RhB/RhB^{+\cdot} \rightarrow \text{other products} \rightarrow CO_2 + H_2O \qquad (10)$$

$$\cdot OH + RhB/RhB^{+\cdot} \rightarrow \text{other products} \rightarrow CO_2 + H_2O \qquad (11)$$

$$h^+ + RhB/RhB^{+\cdot} \rightarrow \text{other products} \rightarrow CO_2 + H_2O \qquad (12)$$

3.9 Regeneration and reusability

It is significant to evaluate the reusable performance and stability of photocatalysts for practical applications.[47] To investigate the stability of Bi_2MoO_6–MIL-100(Fe)-9, we carried out 4 times recycle experiment to degrade RhB under the same conditions. After each cycle, the photocatalyst was centrifuged, filtered, washed and dried at 60 °C for 12 h. As shown in Fig. 10a, after four cycles, the degradation rate of RhB decreased from 88.46% to 84.91%, the photocatalyst removed organic pollutants with only a slight loss of activity. After being used four times, as shown in Fig. 10b, the XRD patterns of Bi_2MoO_6–MIL-100(Fe)-9 composite before and after catalytic reaction further demonstrated that the structure of the Bi_2MoO_6–MIL-100(Fe) composites remain intact. Besides, the ICP-AES analysis showed that the leaching Fe and Bi ions from the photocatalysts in the reaction solution were 0.143 mg L^{-1} and less than 0.01 mg L^{-1} after cycles reaction respectively. The leaching ions concentration is very low compared with the concentration of catalysts (1000 mg L^{-1}), which is negligible. Therefore, the as-prepared Bi_2MoO_6–MIL-100(Fe)-9 composites show excellent stability and reusability in the visible light photochemical applications.

4. Conclusions

In summary, Bi_2MoO_6–MIL-100(Fe) photocatalysts have been successfully fabricated by facile solvothermal method in this work for the first time. The characterizations of Bi_2MoO_6–MIL-100(Fe) composites were confirmed by XRD, SEM/EDS, TEM, and XPS. The as-synthesized Bi_2MoO_6–MIL-100(Fe) photocatalyst exhibited excellent photocatalytic performance in degradation of RhB under visible light. The optimal mass ratio
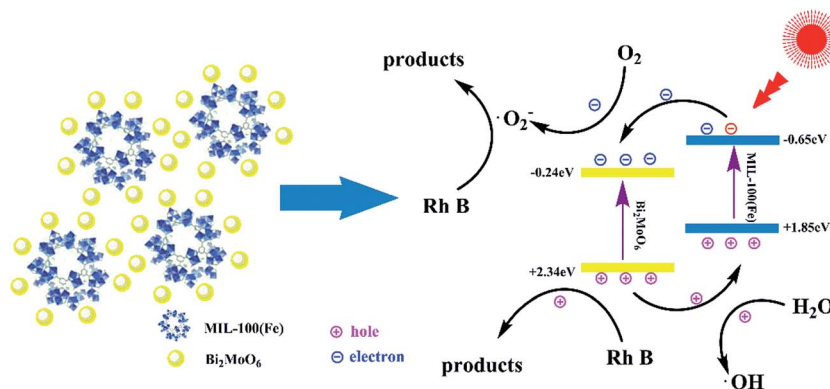
Scheme 1 Photocatalytic degradation mechanism over Bi_2MoO_6–MIL-100(Fe) heterostructure under visible light irradiation.
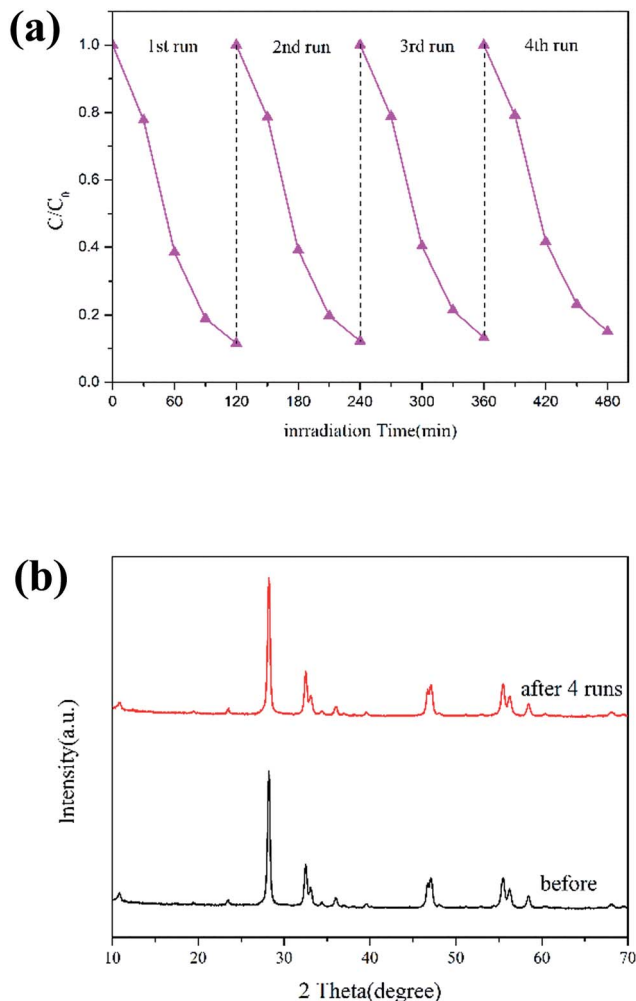
Fig. 10 (a) Cycling runs for photocatalytic degradation of RhB over Bi$_2$MoO$_6$–MIL-100(Fe)-9 under visible light irradiation; (b) XRD patterns of Bi$_2$MoO$_6$–MIL-100(Fe)-9 before and after reactions.

of MIL-100(Fe) in the composite is 9% for the excellent synergistic effect between Bi$_2$MoO$_6$ and MIL-100(Fe). The presence of MIL-100(Fe) in the composites enhanced light absorption, and increased surface area. The photo-generated h$^+$ and $\cdot$O$_2$$^-$ in Bi$_2$MoO$_6$–MIL-100(Fe) composites are proved to be the main active species over the photodegradation. The enhanced photocatalytic performance is mainly attributed to perfect matched energy band of heterostructure, improved photoinduced charge carriers transfer efficiency, and inhibited photo-generated electron–hole recombination. Our study confirmed that the introduction of MIL-100(Fe) into semiconductor Bi$_2$MoO$_6$ can improve the photocatalytic activity and stability of Bi$_2$MoO$_6$-based photocatalysts, it may be a promising candidate in synthesis of novel catalysts.

Acknowledgements

References

1 H. Li, J. Liu, W. Hou, N. Du, R. Zhang and X. Tao, *Appl. Catal., B*, 2014, **160–161**, 89–97.
2 M. Andersson, L. Österlund, S. Ljungström and A. Palmqvist, *J. Phys. Chem. B*, 2002, **106**, 10674–10679.
3 G. Li, X. Nie, Y. Gao and T. An, *Appl. Catal., B*, 2016, **180**, 726–732.
4 Z. F. Yin, L. Wu, H. G. Yang and Y. H. Su, *Phys. Chem. Chem. Phys.*, 2013, **15**, 4844–4858.
5 L. Zhang, T. Xu, X. Zhao and Y. Zhu, *Appl. Catal., B*, 2010, **98**, 138–146.
6 S. Cao, X. Liu, Y. Yuan, Z. Zhang, Y. Liao, J. Fang, S. C. J. Loo, T. C. Sum and C. Xue, *Appl. Catal., B*, 2014, **147**, 940–946.
7 Y. Xu and W. Zhang, *Dalton Trans.*, 2013, **42**, 1094–1101.
8 S. Martha, A. Nashim and K. M. Parida, *J. Mater. Chem. A*, 2013, **1**, 7816.
9 M. Mączka, L. Macalik, K. Hermanowicz, L. Kepiński and J. Hanuza, *J. Raman Spectrosc.*, 2010, **41**, 1289–1296.
10 K. Dai, D. Li, L. Geng, C. Liang and Q. Liu, *Mater. Lett.*, 2015, **160**, 124–127.
11 X. Lin, X. Guo, D. Liu, Q. Wang, H. Zhai and L. Chang, *Mater. Res. Bull.*, 2015, **63**, 72–79.
12 Z. Dai, F. Qin, H. Zhao, J. Ding, Y. Liu and R. Chen, *ACS Catal.*, 2016, **6**, 3180–3192.
13 Y. Feng, X. Yan, C. Liu, Y. Hong, L. Zhu, M. Zhou and W. Shi, *Appl. Surf. Sci.*, 2015, **353**, 87–94.
14 J. Lv, K. Dai, J. Zhang, L. Geng, C. Liang, Q. Liu, G. Zhu and C. Chen, *Appl. Surf. Sci.*, 2015, **358**, 377–384.
15 T. Yan, M. Sun, H. Liu, T. Wu, X. Liu, Q. Yan, W. Xu and B. Du, *J. Alloys Compd.*, 2015, **634**, 223–231.
16 P. Wang, Y. Ao, C. Wang, J. Hou and J. Qian, *Carbon*, 2012, **50**, 5256–5264.
17 A. Phuruangrat, S. Putdum, P. Dumrongrojthanath, N. Ekthammathat, S. Thongtem and T. Thongtem, *Mater. Sci. Semicond. Process.*, 2015, **34**, 175–181.
18 L. Shen, S. Liang, W. Wu, R. Liang and L. Wu, *J. Mater. Chem. A*, 2013, **1**, 11473.
19 M. D. Allendorf, R. J. T. Houk, L. Andruszkiewicz, A. A. Talin, J. Pikarsky, A. Choudhury, K. A. Gall and P. J. Hesketh, *J. Am. Chem. Soc.*, 2008, **130**, 14404–14405.
20 R. B. Getman, Y. Bae, C. E. Wilmer and R. Q. Snurr, *Chem. Rev.*, 2012, **112**, 703–723.
21 P. Horcajada, R. Gref, T. Baati, P. K. Allan, G. Maurin, P. Couvreur, G. Férey, R. E. Morris and C. Serre, *Chem. Rev.*, 2012, **112**, 1232–1268.
22 L. Yang, P. Ravindran, P. Vajeeston and M. Tilset, *Phys. Chem. Chem. Phys.*, 2012, **14**, 4713.
23 I. Luz, F. X. Llabrés I Xamena and A. Corma, *J. Catal.*, 2010, **276**, 134–140.
24 D. Jiang, T. Mallat, F. Krumeich and A. Baiker, *J. Catal.*, 2008, **257**, 390–395.
25 M. Dan-Hardi, C. Serre, T. Frot, L. Rozes, G. Maurin, C. Sanchez and G. Férey, *J. Am. Chem. Soc.*, 2009, **131**, 10857–10859.
26 H. Wang, X. Yuan, Y. Wu, G. Zeng, H. Dong, X. Chen, L. Leng, Z. Wu and L. Peng, *Appl. Catal., B*, 2016, **186**, 19–29.

27 J. He, Z. Yan, J. Wang, J. Xie, L. Jiang, Y. Shi, F. Yuan, F. Yu and Y. Sun, *Chem. Commun.*, 2013, **49**, 6761.

28 F. Ke, L. Wang and J. Zhu, *Nano Res.*, 2015, **8**, 1834–1846.

29 X. Wang, J. Liu, S. Leong, X. Lin, J. Wei, B. Kong, Y. Xu, Z. Low, J. Yao and H. Wang, *ACS Appl. Mater. Interfaces*, 2016, **8**, 9080–9087.

30 D. Esken, S. Turner, C. Wiktor, S. B. Kalidindi, G. Van Tendeloo and R. A. Fischer, *J. Am. Chem. Soc.*, 2011, **133**, 16370–16373.

31 R. Liang, S. Luo, F. Jing, L. Shen, N. Qin and L. Wu, *Appl. Catal., B*, 2015, **176–177**, 240–248.

32 D. Kim, H. Kim and D. Cho, *Catal. Commun.*, 2016, **73**, 69–73.

33 Y. Feng, X. Yan, C. Liu, Y. Hong, L. Zhu, M. Zhou and W. Shi, *Appl. Surf. Sci.*, 2015, **353**, 87–94.

34 Z. Zhao, W. Zhang, Y. Sun, J. Yu, Y. Zhang, H. Wang, F. Dong and Z. Wu, *J. Phys. Chem. C*, 2016, **120**, 11889–11898.

35 H. Li, Q. Deng, J. Liu, W. Hou, N. Du, R. Zhang. T. Xutang, 2014.

36 F. Zhang, Y. Jin, J. Shi, Y. Zhong, W. Zhu and M. S. El-Shall, *Chem. Eng. J.*, 2015, **269**, 236–244.

37 L. Shen, S. Liang, W. Wu, R. Liang and L. Wu, *J. Mater. Chem. A*, 2013, **1**, 11473.

38 D. Yue, T. Zhang, M. Kan, X. Qian and Y. Zhao, *Appl. Catal., B*, 2016, **183**, 1–7.

39 J. Lv, K. Dai, J. Zhang, L. Geng, C. Liang, Q. Liu, G. Zhu and C. Chen, *Appl. Surf. Sci.*, 2015, **358**, 377–384.

40 S. Fang, C. Ding, Q. Liang, Z. Li, S. Xu, Y. Peng and D. Lu, *J. Alloys Compd.*, 2016, **684**, 230–236.

41 J. Cao, B. Xu, H. Lin, B. Luo and S. Chen, *Dalton Trans.*, 2012, **41**, 11482.

42 X. Xiong, L. Ding, Q. Wang, Y. Li, Q. Jiang and J. Hu, *Appl. Catal., B*, 2016, **188**, 283–291.

43 Y. Yao, J. Qin, H. Chen, F. Wei, X. Liu, J. Wang and S. Wang, *J. Hazard. Mater.*, 2015, **291**, 28–37.

44 R. Jiang, H. Y. Zhu, J. B. Li, F. Q. Fu, J. Yao, S. T. Jiang and G. M. Zeng, *Appl. Surf. Sci.*, 2016, **364**, 604–612.

45 J. Tian, P. Hao, N. Wei, H. Cui and H. Liu, *ACS Catal.*, 2015, **5**, 4530–4536.

46 X. Yuan, H. Wang, Y. Wu, G. Zeng, X. Chen, L. Leng, Z. Wu and H. Li, *Appl. Organomet. Chem.*, 2016, **30**, 289–296.

47 S. Martha, A. Nashim and K. M. Parida, *J. Mater. Chem. A*, 2013, **1**, 7816.